



# Physical study of the 3-dimensional characteristics and free-surface properties of a breaking roller in bores and surges

Davide Wüthrich\*, Rui Shi, Hubert Chanson

The University of Queensland, School of Civil Engineering, Brisbane, QLD 4072, Australia

## ARTICLE INFO

### Keywords:

Positive surge  
Breaking bore  
Aeration  
Roller toe  
Bore celerity  
Open channel

## ABSTRACT

Breaking surges and bores are observed during flood events, tidal bores and tsunamis propagating in rivers. The sudden increase in water depth generates an aerated and recirculating region, called the roller, whose turbulent behaviour is poorly understood. Based on ensemble-average analyses with multiple repetitions, this experimental work processed high-speed videos from multiple locations to characterise the spatial and temporal dynamics of the bore's roller. The results showed different air entrainment mechanisms for increasing Froude numbers, providing adapted formulae to predict the extension of the shear layer and the air-water boundary. Seen from above, the roller toe perimeter had an indented profile rapidly evolving in time, revealing a certain level of periodicity. A statistical analysis in terms of position of the roller toe, longitudinal fluctuations and instantaneous celerities allowed for a detailed characterisation of the turbulent surface fluctuations and three-dimensional properties of the breaking bore roller, leading to a better understating of the governing process.

## 1. Introduction

A positive surge, also called bore or compression wave, may be described as a translating hydraulic jump [15], and it visually appears as a sudden increase in water depth. The characteristics of the surge front are defined by the bore Froude number:

$$Fr_1 = \frac{V_1 + U}{\sqrt{g \cdot d_1}} \quad (1)$$

where  $V_1$  is the initial velocity,  $U$  is the bore celerity,  $g$  is the gravitational acceleration ( $g = 9.8 \text{ m/s}^2$ ) and  $d_1$  is the initial flow depth. For  $Fr_1 > 1.4$ – $1.5$ , the bore propagation becomes a highly turbulent process with the formation of a fully breaking roller, characterised by substantial air entrainment, strong free-surface dynamics and turbulent air-water interactions.

Despite their different generation mechanisms, positive surges are widely observed in nature and man-made environment, including rejection surges in canals and rivers downstream of hydropower plants, flood waves, tidal bores (Fig. 1), dam-break waves and tsunamis propagating in rivers. Early studies on positive surges mostly focused on theoretical considerations and experimental investigations of the free-surface characteristics, including the works of Favre [11], Benjamin and Lighthill [2], Peregrine [32], Benet and Cunge [1] and Wilkinson and Banner [39]. Since the 1990s, with the development of data acquisition

systems and signal processing techniques, comprehensive physical modelling was undertaken focusing on the turbulence characteristics and free-surface properties. Some experimental breakthroughs included the turbulence characterisation using Particle Image Velocimetry (PIV) in a translating hydraulic jump [16], sedimentation process in tidal bores [18], turbulent integral scales in tidal bores [22–23] and tsunami-induced bores propagating in rivers [41]. Positive surges were also the subject of numerous numerical studies [27,31,26,25,24] and field investigations [9,10,33,34].

While these contributions provided a better insight of flow mechanisms in positive surges, some challenges in the understanding of the unsteady two-phase turbulence, the air-water flow properties and free surface characteristics associated with the intensive interfacial interactions still remain. Limited works presented quantitative air-water measurements, mainly focused on the void fraction [30,3,23]. On the other hand, many researchers attempted to establish relationships between the free-surface dynamics and the inner turbulent behaviour [12,14,4,5,35,44]. For stationary hydraulic jumps, the free surface dynamics were intensively investigated in the past [6,28,29,43,38]. However, for breaking bores, only the experimental work of Leng and Chanson [20,21] documented coarsely some free-surface properties of translating rollers, including bore celerity and instantaneous longitudinal and transversal free-surface fluctuations. Thus, there is a clear need for some fundamental studies on the characterisation of breaking

\* Corresponding author.

E-mail addresses: [d.wuthrich@uq.edu.au](mailto:d.wuthrich@uq.edu.au) (D. Wüthrich), [rui.shi@uq.net.au](mailto:rui.shi@uq.net.au) (R. Shi), [h.chanson@uq.edu.au](mailto:h.chanson@uq.edu.au) (H. Chanson).



Fig. 1. Tidal bore in the Qiantang River (China) on 11/10/2014 between Yanguan and Laoyanchang (photo by H. Chanson, Digital Camera Pentax K-7 & FA \* 300 mm  $f$ 4.5).

rollers in surges and bores. These will support the understanding of free-surface dynamics, as well as broadening the experimental databases used to validate numerical results in the future.

In this context, the present study presents a new series of detailed physical experiments on the free-surface characteristics of positive surges with breaking rollers. More specifically this research:

- introduces a novel, non-intrusive, image processing technique of high-speed video data based on a large number of repetitions;
- provides a detailed and comprehensive characterisation of the bore's breaking roller in terms of air entrainment mechanisms, longitudinal free-surface profiles and fluctuations, roller toe perimeters and instantaneous celerity;
- discusses the three-dimensional (3D) nature of the turbulent bore front and its temporal periodicity.

## 2. Experimental set-up

All tests were carried out at the University of Queensland, Australia. The tilting channel had a length of 19 m and width of 0.7 m with smooth PVC bottom and transparent side glasses. Bores were generated through the sudden closure of a downstream Tainter gate, inducing a positive surge propagating in the upstream direction, as shown in Fig. 2. For all configurations the flow had a discharge of  $Q = 0.101 \text{ m}^3/\text{s}$ , resulting in the flow conditions detailed in Table 2. In terms of instrumentations, the discharge was controlled with a magneto flow meter with an accuracy of  $10^{-5} \text{ m}^3/\text{s}$ . Flow depths were measured using non-intrusive Acoustic Displacement Meters (ADM) type Micro-sonic™ Mic + 25/IU/TC, calibrated in situ and sampled with a frequency of 200 Hz, an accuracy of 1% and a spatial resolution of

0.1 mm. The bore front celerity was computed as  $U = \Delta x/\Delta t$  between adjacent ADM sensors, whose positioning is illustrated in Fig. 2.

A Phantom high-speed digital camera (v2011) was used to capture the motion within the propagating bores, recording up to 22,700 monochrome frames per second (fps) in full high definition ( $1280 \times 800$  pixels) or  $10^6$  fps in low-definition ( $128 \times 16$  pixels). In the present study, the movies were recorded at 22,000 fps in high definition ( $1280 \times 800$  pixels) (Table 1). The camera was installed both on the side (Section 4) and on top (Section 5) of the channel, as shown in Fig. 3. All videos were recorded at a reference location  $x = 8.5 \text{ m}$  from the channel inlet, in line with previous studies (Leng and Chanson [20,21]). For the side view experiments, the Phantom video-camera was equipped with a lens Zeiss™ Planar T\*85 mm  $f$  1.4, located at a distance of  $\sim 1.5 \text{ m}$  from the channel side wall, allowing a measuring window of  $0.52 \times 0.32 \text{ m}$ , resulting in a pixel resolution of 0.4 mm. For the top view the Phantom video-camera was installed above the channel (perpendicular to the channel flow), equipped with a lens Nikon™ AF 50 mm  $f$  1.4, located at a distance of  $\sim 1.3 \text{ m}$  from the flow surface, allowing to capture all its width with a measuring window of  $0.7 \times 0.45\text{--}0.52 \text{ m}$ . This resulted in a pixel resolution ranging from 0.60 to 0.65 mm. Both lenses had a negligible level of distortion and video recording was performed with a Light Emitting Diode (LED) array to maximize the visibility of the flow features (Fig. 3a). The propagation of the bore was weakly affected by the presence of the sidewalls, thus suggesting minimal model effects. Examples of the recorded videos are presented Supplementary material in Appendix B.

The present study is based on a Froude similitude, thus guaranteeing that the ratio between gravitational and inertial forces is conserved at all scales. The Reynolds number  $Re_1 = \rho \cdot (V_1 + U) \cdot d_1 / \mu$  was sufficiently high to minimise scale effects and the Morton number  $Mo = g \mu^4 / (\rho \sigma^3)$  becomes an invariant for air-water flows, thus assuring a good reproducibility of the phenomena involved (Table 2). More details on scale effects in bores and positive surges are provided by Leng and Chanson [22].

## 3. Methodology

### 3.1. Experimental program

This research project is based on an experimental approach with a large number of repetitions, yielding ensemble-averaged and instantaneous fluctuation properties. Details on the experimental program are presented in Table 1. This study focused on turbulent breaking bores with Froude numbers ranging between 1.5 and 2.4. For the same incoming discharge ( $Q = 0.1 \text{ m}^3/\text{s}$ ), higher Froude numbers were obtained increasing the channel slope, ensuring that the bore did not present a decelerating behaviour. Given the unsteadiness of the process, a number of  $R$  repetitions was performed and results statistically

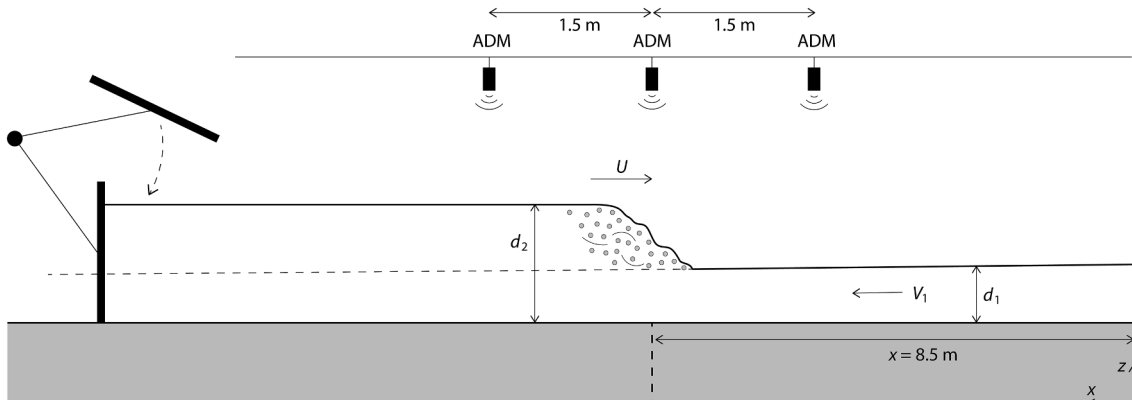
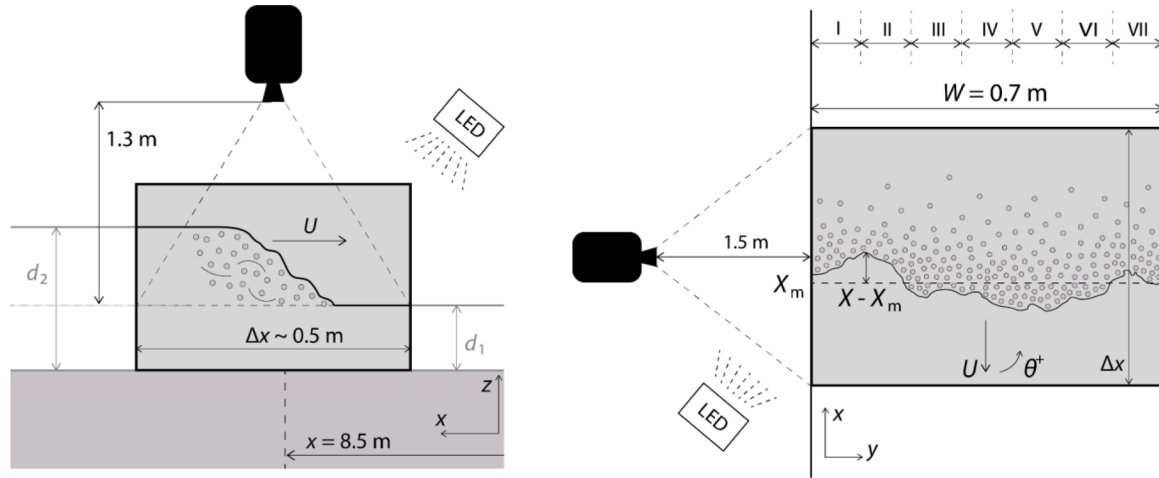


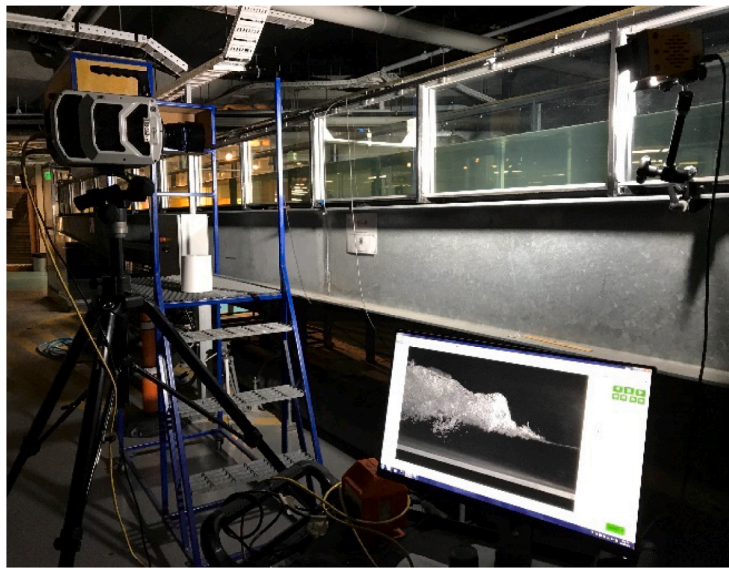
Fig. 2. Experimental set-up for bore generation and definition of the parameters.

**Table 1**  
Experimental program of the High-Speed video camera.

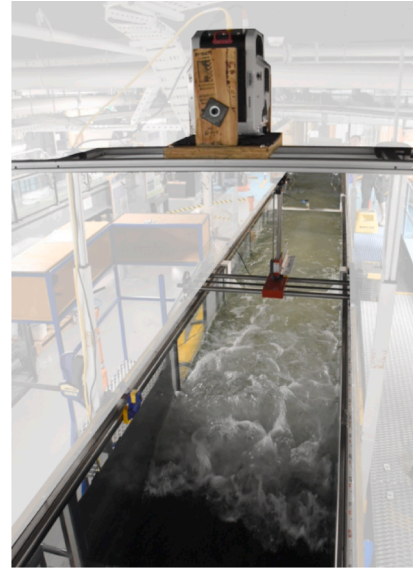
	Fr <sub>1</sub>	Slope[%]	Nb of videos	Acquisition frequency before filtering	Resolution [pixels]	Acquisition frequency after filtering	Total processed frames	Lens aperture/ exposure	Video in Appendix B
Top	1.5	0	25	22,000 fps	1280 × 800	1000 fps	13,152	2.0/40 μs	Bore_Top_1
	2.1	0.75							Bore_Top_2
	2.4	1.25							Bore_Top_3
Side	1.5	0	8						Bore_Side_1
	2.1	0.75							Bore_Side_2
	2.4	1.25							Bore_Side_3



(a) definition sketch of the position of the video camera and main parameters: top view experiments (left) and side view experiments (right).



(b) Part 1 – Side view experiment



(c) Part 2 – Top view experiment

**Fig. 3.** Position of the high-speed video camera and definition sketch of top and side view experiments.

**Table 2**  
Physical properties of the breaking bores.

Fr <sub>1</sub>	Re	Mo	S <sub>0</sub> [%]	Q [m <sup>3</sup> /s]	d <sub>1</sub> [m]	V <sub>1</sub> [m/s]	U [m/s]	d <sub>2</sub> [m]	Repetitions
1.51	3.21 · 10 <sup>5</sup>	1.6 · 10 <sup>-11</sup>	0.00	0.1	0.168	0.848	1.061	0.283	25
2.15	2.03 · 10 <sup>5</sup>	1.6 · 10 <sup>-11</sup>	0.75	0.1	0.097	1.468	0.627	0.244	25
2.45	1.86 · 10 <sup>5</sup>	1.6 · 10 <sup>-11</sup>	1.25	0.1	0.084	1.707	0.504	0.245	25

analysed in terms of ensemble average and fluctuations, in the form:

$$\bar{X} = \frac{1}{R} \sum_{i=1}^{i=R} X_i \quad (2)$$

Based on previous results by Leng and Chanson [20,21], repetitions varied between  $R = 8$  for the side view to  $R = 25$  for the top view data sets.

Channel slopes ranged between 0 and 1.25%, generating flows with different hydrodynamic properties and bores with various Froude numbers  $Fr_1$  (Eq. (1)). The main physical properties of the generated bores for all Froude numbers are summarised in Table 2. For each Froude number a side-view and a top-view videos are presented as Supplementary material in Appendix B, with details provided in Table B.1.

### 3.2. Image processing

For both top and side views, video processing was performed by means of a gradient-based algorithm, capable of extracting boundaries of the air-water flow region in breaking bores from each individual frame. For the **side view**, this algorithm consisted of four main steps: (1) a raw image was extracted from the high-speed video movies, with lens distortion minimised using the Camera Calibration Toolbox; (2) a Gaussian smoothed raw image was subtracted to remove background information; (3) the spatial gradient magnitude of the image was computed, detecting the distinctive discontinuities of the brightness in the air-water interfaces; (4) the median filtering was then applied to minimise noise whilst preserving the edges. Based on the significant increase in gradient magnitude, a “*boundary recognition*” algorithm was developed to extract the upper and lower boundaries of the air-water region. For the detection of the roller toe perimeter in the **top view** (Section 5), steps (1) and (3) were identical, whilst step (2) was not necessary due to the lack of background information. Furthermore, a modified step (4) was applied to remove noise in the form of reflections of the free-surface and local drop ejections. Evidently, for the top view analysis only the upper boundary was identified. Some typical results obtained for both side and top views are shown in Fig. 4, proving that the algorithm was able to precisely identify the air-water regions. The precision of the edge-detecting algorithm directly depended on the pixel size, which ranged from 0.4 to 0.6 mm. It is important to point out that the subtraction of the Gaussian smoothing did not promise 100% background removal, but only the *out-of-focus* background information. In addition, the median filtering inevitably removed some fine details on the edges, but this had a negligible effect on the data analysis.

## 4. Breaking roller: Side view characteristics

From a side view, a breaking bore is characterised by intensive three-dimensional turbulence with large vortical structures, a highly fluctuated free-surface, air bubble entrainment at the roller toe and intense splashing. Fig. 5 presents the air entrainment of breaking rollers

propagating from the right to left. Videos of the propagating bores are provided supplementary material in Appendix B. The interaction of the initial steady flow with the propagating bore induced an upward movement of the free surface, causing a discontinuity where a large amount of air pockets were entrained. The immediate downstream point of impingement is defined *roller toe*, which initialised the air entrainment process and vortex generation. The vorticity within the roller enhanced the roller free-surface deformation and air-water mixing process, resulting in various air entrainment mechanisms, detailed hereafter.

### 4.1. Air entrainment mechanisms

Leng [19] observed an undular bore for  $Fr_1 = 1.1$ – $1.5$  and a breaking bore for  $Fr_1 > 1.5$ – $1.6$ . The flow visualization showed that, for  $Fr_1 = 1.2$ – $1.3$ , a small roller was formed at the first crest of undulation with air entrainment inception. The high-speed movies provided detailed insight into the air entrainment processes of breaking bores with Froude numbers  $Fr_1 = 1.5$ , 2.1 and 2.4, pointing out some differences in air entrainment mechanisms with increasing  $Fr_1$ , as illustrated in Fig. 6.

The breaking bore with  $Fr_1 = 1.5$  featured an upward curvature immediately ahead of the bore front, an air entrainment region higher than the initial free-surface and the absence of flow recirculation within the roller (Figs. 4a, 5a and movie Bore\_Side\_1 in Supplementary material Appendix B). Two air entrainment mechanisms were observed herein, as shown in Fig. 6a. The first was linked to the local change in flow direction at the roller toe where a periodic plunging process was induced, entrapping large air pockets. The second was induced by the air layer above the initial free-surface, travelling with the same velocity of the initial steady flow. The air layer impinged into the longitudinal direction and was enclosed by shear force and water gravity. The intense turbulence and free-surface deformation within the roller were responsible for the breaking of the entrained air pockets into smaller-size bubbles, subsequently advected in the shear layer until they travelled upwards to the free surface. For  $Fr_1 = 1.5$ , the shear layer was located above the initial free surface. This was attributed to the absence of large vertical structures and to a predominant bubble motion driven by buoyancy.

Contrarily, for the bores with relatively large Froude number ( $Fr_1 = 2.1$  and 2.4), the roller featured more intense air-water interactions, the presence of large vortices and intense free-surface fluctuations with random projection of droplets above the free-surface (Figs. 5b, 6b and movies Bore\_Side\_2 and Bore\_Side\_3 in Supplementary material Appendix B). Unlike the bore with lower Froude numbers, the impingement point at the roller toe was not the only source of air entrainment. Large-scale turbulent structures formed at the roller toe associated with the Kelvin-Helmholtz instabilities, and evolved within the shear layer, inducing important free-surface deformations responsible for air entrainment through roller rotation, collision of adjacent vortices

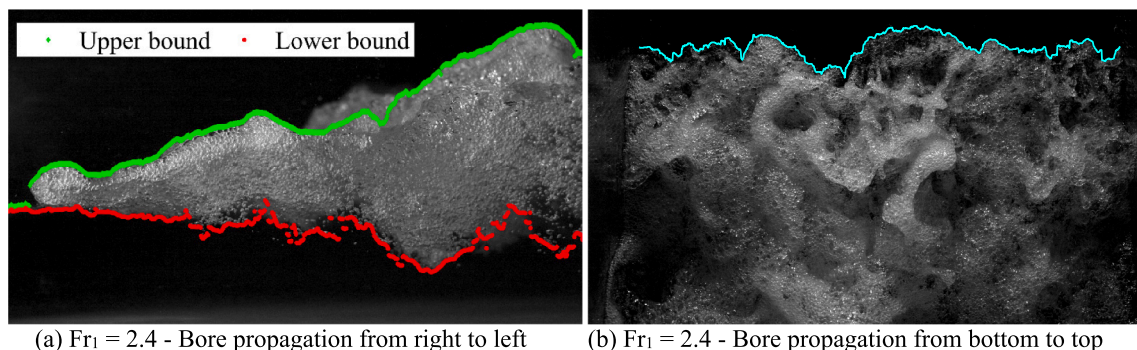


Fig. 4. Edge detection techniques of the air-water region in breaking bores: (a) side view; (b) top view.

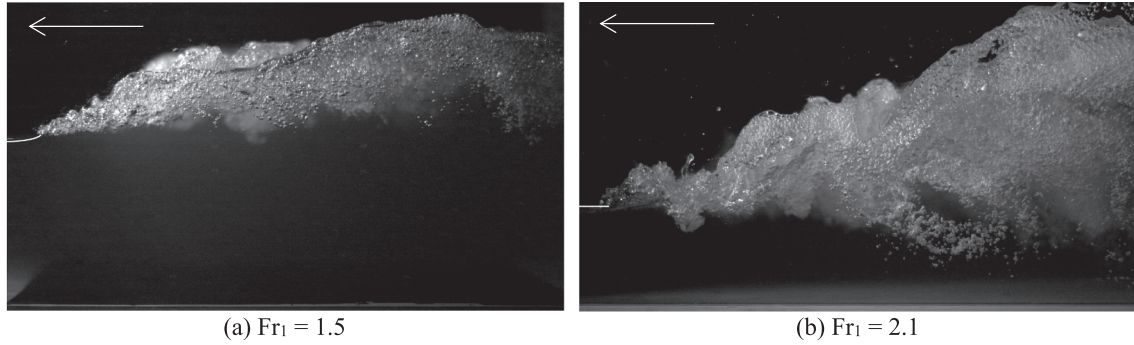


Fig. 5. Side views of air entrainment in breaking rollers captured using a high-speed video camera. ( $Q = 0.101 \text{ m}^3/\text{s}$ , initial flow from left to right with bore propagating in opposite direction).

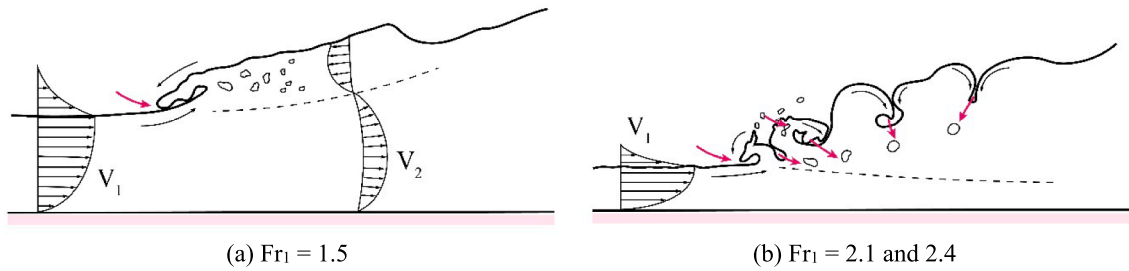


Fig. 6. Schematic representation of air entrainment mechanisms in breaking bores with different Froude numbers.

at the surface, splashes and droplets impact (Fig. 6b and movies Bore\_Side\_2 and Bore\_Side\_3 in Supplementary material Appendix B). The intense free-surface fluctuations also entrapped air pockets within the shear layer, which developed below the free-surface of the initial steady flow.

#### 4.2. Air-water boundaries

A definition of the upper and lower boundaries of the shear layer within the roller is important for a comprehensive characterisation of a breaking bore's behaviour. For this, both boundaries were tracked using the image processing algorithm introduced in Section 3.2. All videos for all Froude numbers were synchronised at the location of the roller toe ( $x = 0$ ) and the boundaries of air-water regions ensemble-averaged over all repetitions. Results are presented in Fig. 7.

The lower air-water boundary of the roller coincided with the deepest extension of the shear layer, representing a substantial difference in density between the highly aerated region on the upper side and the water layer underneath. Following the approach of Hoyt and Sellin [17], the lower air-water boundary (*i.e.* the extension of the turbulent shear layer) can be locally approximated by a linear function:

$$\frac{z}{d_1} = 1 + n \cdot \left( \frac{x - x_{\text{toe}}}{d_1} \right) \quad (3)$$

valid in the roller length region  $0 < x - x_{\text{toe}} < L_r$ , where  $L_r$  is the roller length, defined as the distance between the roller toe and the end of the breaking roller, marked by a monotonic increase in free-surface elevation until the conjugate depth  $d_2$  [13,36,19]. Because of the development of Kelvin-Helmholtz vortices, for  $Fr_1 > 2.0$ , the elevation of the lower boundary tended to decay with increasing longitudinal distance, leading to an empirical coefficient  $n = -0.064$  (Fig. 5b and movies Bore\_Side\_2 and Bore\_Side\_3 in Supplementary material Appendix B). For  $Fr_1 = 1.5$ , the boundary elevation of the breaking shear layer increased from the impingement point, leading to a value of  $n = 0.064$  (Fig. 5a and movie Bore\_Side\_1 in Supplementary material Appendix B). Apart from the longitudinal advection and diffusion of the entrained air bubbles from the roller toe, the bubbles were

superimposed on an upward motion shortly after the bore passage ( $(x - x_{\text{toe}})/d_1 > 0.3$ , where the turbulent dissipation allowed buoyancy to drive the bubble motion).

The upper air-water boundary represented the location of the free-surface, exhibiting a self-similar profile. Similarly to the lower boundary, the slope of the bore front could be initially approximated by a linear function (Eq. (3)) within the interval  $0 < (x - x_{\text{toe}})/d_1 < 0.5L_r$  with  $n = 0.48$  for  $Fr_1 = 1.5$  and  $n = 0.40$  for  $Fr_1 > 2$ . In addition, the ADM data provided an instantaneous time variation of free surface evolution at a fixed location. The ADM data were translated to a spatial domain using the average celerity of the bore front ( $x = Ut$ ), and used to compare the free-surface profiles obtained from the image processing technique. All data are presented in Fig. 7, showing some good agreement between the two approaches, *i.e.* video imaging and ADM. The mean self-similar free surface profile can be expressed as an empirical function:

$$\frac{d - d_1}{d_2 - d_1} = \left( \frac{x - x_{\text{toe}}}{L_r} \right)^N \quad (4)$$

where  $d$  is the ensemble-averaged depth,  $d_1$  is the initial water depth,  $d_2$  is the tailwater conjugate depth,  $L_r$  is the bore roller length,  $x_{\text{toe}}$  is the longitudinal location of roller toe, and  $N$  is an empirical exponent herein defined as  $N = 0.44$  for breaking bores with  $Fr_1 = 1.5$  and  $N = 0.54$  for  $Fr_1 > 2.0$  (Fig. 7). These results are in line with previous studies that showed  $N = 0.44\text{--}0.54$  for stationary hydraulic jumps [7,37],  $N = 0.60$  in breaking bores [8], and  $N = 0.48$  for tsunami-like waves over wet bed [40].

The fluctuating nature of both upper and lower boundaries of the air-water flow region is presented in Fig. 8 for a selected bore with  $Fr_1 = 2.1$ . Similar behaviours were overserved for the other Froude numbers, but not detailed herein. The fluctuations were defined as the difference between the third and first quartile ( $d_{75} - d_{25}$ ) of the statistical data-set derived from all videos. The upper boundary, *i.e.* the free-surface, fluctuated with a nearly constant value  $(d_{75} - d_{25})/d_1 \sim 0.2$ . Contrarily, the fluctuations of the lower bound increased whilst moving away from the roller toe, with a maximum value of  $(d_{75} - d_{25})/d_1 = 0.8$  at  $x/d_1 = 4.25$ . Such increase was consistent with the

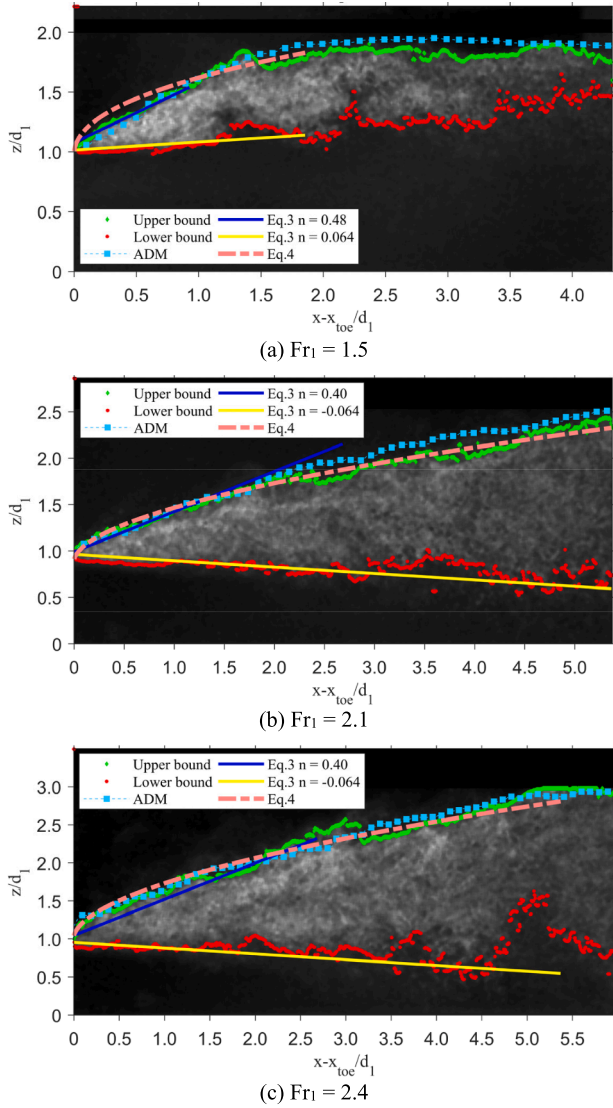


Fig. 7. Ensemble-averaged upper and lower boundaries of the air-water region in breaking bores with: (a)  $Fr_1 = 1.5$  (b)  $Fr_1 = 2.1$  and (c)  $Fr_1 = 2.4$ . ADM data were plotted to compare the results of the image processing technique.

development of large turbulent air-water structures through vortex pairing and shedding. Towards the end of the roller, the decrease in turbulent kinetic energy from the large vortices led to a change in physical process and air bubbles originally advected were affected by random buoyancy-driven motions.

## 5. Breaking roller: Top view characteristics

The roller toe perimeter represents the boundary between the initially steady flow and the bore front propagating upstream. Seen in elevation, the impinging perimeter of a breaking bore is easily recognizable as the transition between the white air-water mixture and the initially clear water (Fig. 4a and movies Bore\_Top\_1, Bore\_Top\_2 and Bore\_Top\_3 in Supplementary material Appendix B). Herein the perimeter of the roller toe was obtained at every frame through the gradient-based algorithm described in Section 3.2. An example of instantaneous profiles obtained for a bore with  $Fr_1 = 2.4$  is presented in Fig. 9 for a frequency of 200 fps. In Fig. 9, the reference point is located at the bottom left corner of the image. The zero temporal value is set when an initial portion of the roller toe enters the measurement window. One can notice that its shape continuously changed in both

time and space. The detailed availability of high-quality data at 1000 fps allowed for more in-depth investigations in terms of the position of the median front and its fluctuations, the instantaneous celerity, the spatial orientation of the front propagation and its pseudo-periodic features.

### 5.1. Position of roller toe

For each profile  $X(t)$  shown in Fig. 9, the instantaneous position of the roller toe was characterised in terms of its median values  $X_m$  and fluctuations  $X'$ , such that:

$$X' = X - X_m \quad (5)$$

In the present study, the statistical median value was chosen over the arithmetic mean to minimise the influence of extreme values.  $X_m$  was computed for each profile and the results are plotted as a function of the normalised time in Fig. 10a and 10b for selected Froude numbers ( $Fr_1 = 1.5$  and 2.4), and ensemble-averaged over 25 repetitions. The grey areas in Fig. 10 indicate the intervals during which the roller toe perimeter is incomplete within the measurement window. Results showed consistent profiles for all tests. A difference between  $Fr_1 = 1.5$  and 2.4 can be observed in terms of fluctuations to the median values, suggesting a more oscillating and turbulent behaviour associated with higher Froude numbers. Results similar to  $Fr_1 = 2.4$  were obtained for  $Fr_1 = 2.1$ , as detailed in Appendix A (Figure I.2). For larger Froude numbers, the temporal evolution showed some backshifts with locally negative celerity values, previously documented by Leng and Chanson [20,21]. These are the result of complex and currently unexplained turbulent processes within the roller toe, including local flow ejections, re-entrant jets and air entrapment. Local backshifts motions can be observed in movies Bore\_Top\_2 and Bore\_Top\_3 in the supplementary material Appendix B and were strongly linked with the roller's inner recirculation process, suggesting the existence of a cyclic behaviour with a temporal periodicity. In addition, the experimental data was successfully compared to the position of an idealised bore front moving with a constant average celerity  $U_{ADM}$ , captured by the ADM sensors (Table 2). The comparison showed consistency between the two approaches. The behaviour of the roller toe in the transversal direction was further detailed herein. The data were analysed for 7 sub-sections of the channel with a width of 0.1 m each (Fig. 3a) and presented in Fig. 10c for  $Fr_1 = 2.4$ . The results were compared to the ensemble-averaged values obtained over the whole channel width, showing no major differences between the different sections, thus confirming the uniformity of the roller in the transversal direction. A comparison between the position of the roller obtained from the top and side views is further shown in Fig. 11. The good agreement between both data sets and the ADM measurements for all Froude numbers showed consistency between these different approaches. More scattering can be observed for the side view data due to the lower number of repetitions available.

The instantaneous longitudinal fluctuations of the roller toe from the median bore front were computed for every profile  $i$  as  $X' = X - X_m$  (Eq. (5)) and their statistical distribution is presented in Fig. 12 for all tested Froude numbers. Results showed some Probability Distribution Functions (PDF) characterised by a pronounced peak at  $X' = 0$  for all flow conditions. The dimensionless standard deviation  $(X - X_m)/d_1 = 0.15$  computed for  $Fr_1 = 1.5$  was in close agreement with that previously presented by Leng and Chanson [20,21] for the Qiantang River bore  $((X - X_m)/d_1 \sim 0.13)$ . However, for stronger bores, the standard deviation increased to 0.36 for  $Fr_1 = 2.1$  and 0.37 for  $Fr_1 = 2.4$ , highlighting a more fluctuating behaviour associated with larger Froude numbers. This is confirmed by the difference between the third and first quartiles  $(X - X_m)_{75} - (X - X_m)_{25}$  providing an insight of turbulent inner length scales ranging from 0.030 m for the weaker bore ( $Fr_1 = 1.5$ ) to 0.043 m for the stronger bore ( $Fr_1 = 2.4$ ). The PDFs obtained from the experimental data were also compared in Fig. 12 to a normal distribution with identical mean and standard deviation values.

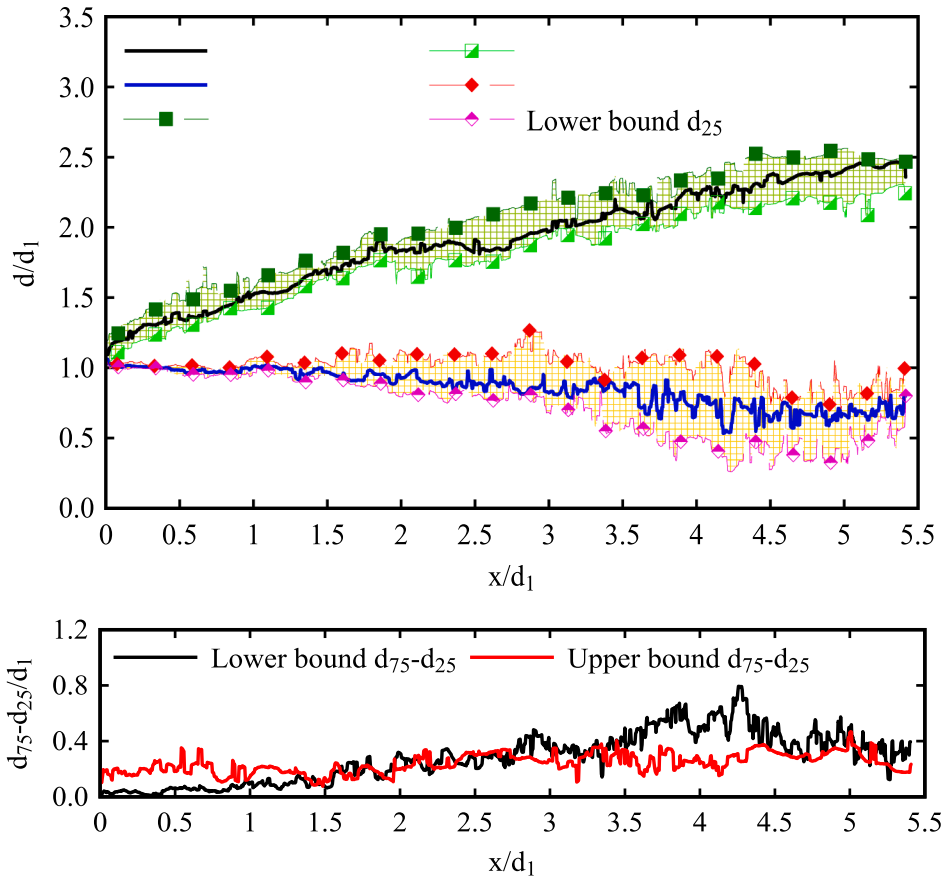


Fig. 8. Fluctuations of upper and lower boundaries of the air-water region for breaking bores with  $Fr_1 = 2.1$ .

Results showed that the bore front fluctuations had a behaviour fairly similar to the Gaussian bell-shape for all tested Froude numbers. The relatively low values of the skewness indicated a symmetrical behaviour of the distribution with respect to the median values. Overall, the data obtained with the high-speed videos showed distributions that

were in agreement with those previously reported by Leng and Chanson [20] for  $Fr_1 = 1.33-1.50$  and the field data collected in Qiantang River bore ( $Fr \sim 2.1$ ) [20].

Similarly to Fig. 10c the instantaneous fluctuations of the roller toe  $X'$  were computed over 7 sub-sections of the channel ( $\Delta y = 0.1$  m).

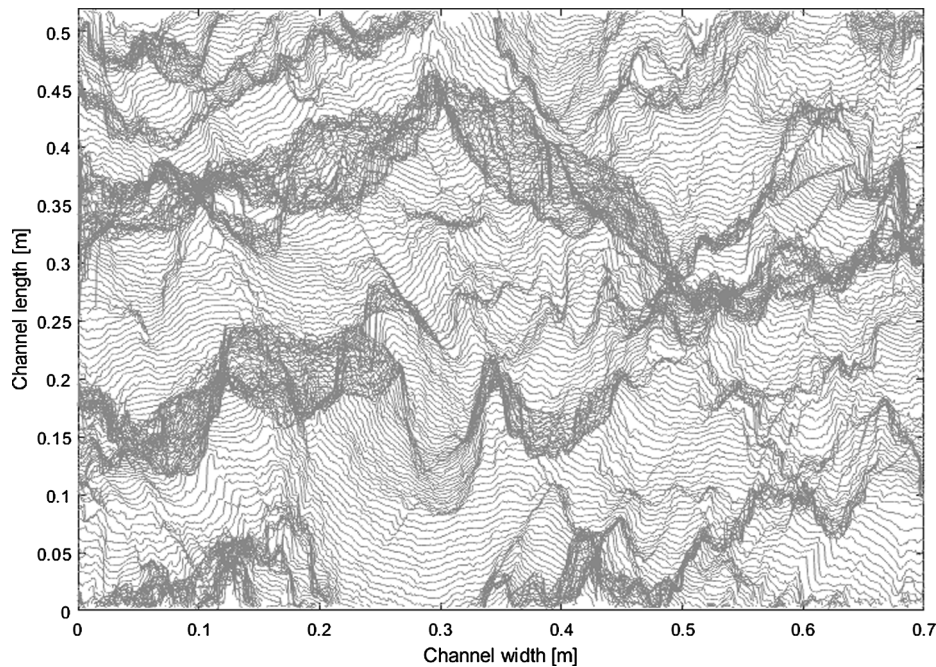


Fig. 9. Instantaneous roller toe perimeters (subsamped at 200 fps) bore propagating from top to bottom ( $Fr_1 = 2.4$ ).

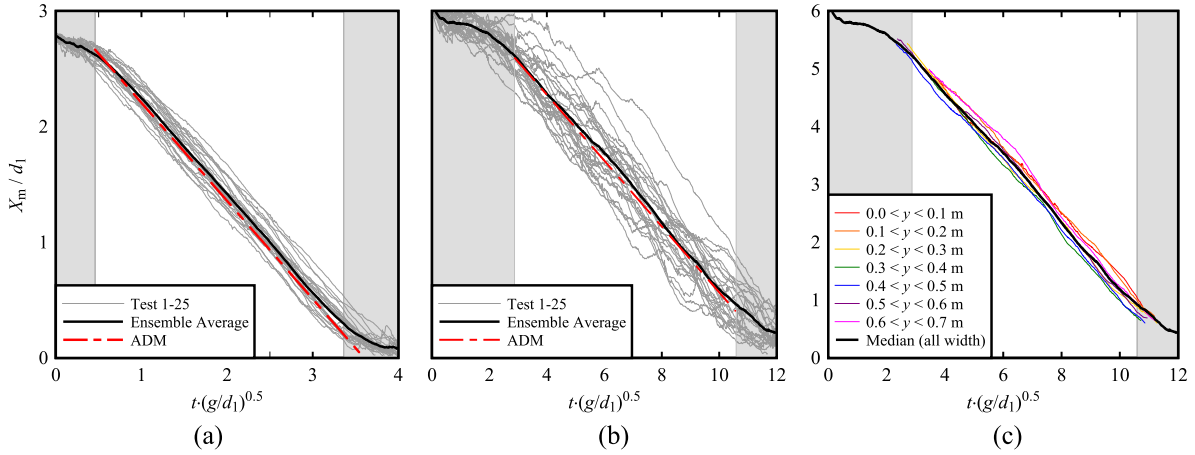


Fig. 10. Position of the roller toe for different Froude numbers: (a)  $Fr_1 = 1.5$ , all channel width; (b)  $Fr_1 = 2.4$ , all channel width; (c)  $Fr_1 = 2.4$ , transversal subsections of 0.1 m each.

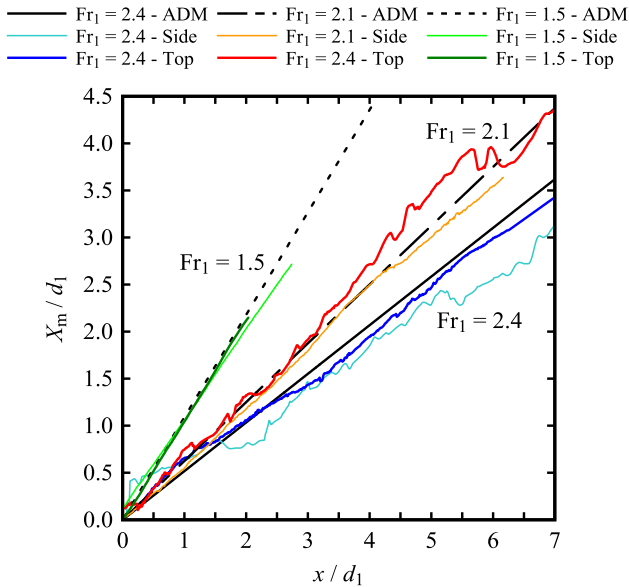


Fig. 11. Position of the roller toe: comparison between top view data, side view and ADM measurements.

Their Probability Distribution Functions are presented in Figure I.2 (see Appendix A and Supplementary material) for all Froude numbers, showing no difference in bore roller behaviour in the transversal direction. This implies that the fluctuations of the roller toe are constant along the channel width, thus suggesting a homogeneous turbulent behaviour across the transversal cross-section. These results also pointed out no sidewall effects, in agreement with Fig. 10c. A similar analysis was conducted for all other Froude numbers ( $Fr_1 = 1.5$  and 2.1), yielding similar conclusions, as presented in Supplementary material Appendix A.

To better quantify the behaviour of the roller toe, an indentation coefficient  $I_C$  was defined as the ratio between the length of the toe perimeter and the channel width (*i.e.*  $W = 0.7$  m). It follows that a higher value of  $I_C$  corresponds to a more indented profile, whereas the value  $I_C = 1$  would correspond to an idealised straight line, perpendicular to the channel axis. Results are presented in Fig. 13, showing mean values around 1.7–1.75 for all bores, with slightly larger values for increasing Froude numbers. It is believed the higher values of  $I_C$  are a consequence of a stronger inner turbulence associated with higher Froude numbers. Because of the short duration of the signal, no periodicity was detected in the temporal evolution of  $I_C$ .

The video analyses showed in-plane movements of the roller toe, deviating from the longitudinal trajectory. An indication of the instantaneous local direction of the bore front was obtained by dividing each profile into segments of 25 pixels, *i.e.*  $\sim 16$  mm at model scale, and applying a spatial (in-plane) cross-correlation analysis between two successive segments. The instantaneous and local direction of the profile was then obtained as:

$$\theta = \tan^{-1}\left(\frac{\Delta X}{\Delta Y}\right) \quad (6)$$

where  $\Delta X$  was obtained as the difference between the median value of each segment and  $\Delta Y$  the transversal distance associated with the maximum cross-correlation. If  $\Delta X < 0$ , the bore front was locally moving upstream (backshift) with a direction  $|\theta| > 90^\circ$  (Fig. 3a). The normalised PDFs of  $\theta$  are presented in Fig. 14 in the form of a polar chart. All flow conditions showed a pronounced peak for  $\theta = 0^\circ$  with decreasing values in a symmetrical behaviour on both the positive and negative directions. Results also pointed out that higher Froude numbers were associated with larger spreading angles, thus suggesting a more intense bi-dimensional behaviour with recirculating patterns in the horizontal  $x$ - $y$  plane. Furthermore, for  $Fr_1 = 1.5$  very few negative values of  $\theta$  were observed, suggesting limited upstream motions, in agreement with the findings presented in Fig. 10a. In contrast, breaking rollers with larger  $Fr_1$  were associated with more intense backwards motions, as previously pointed out in Fig. 10b. Overall, the results confirmed the quasi-two-dimensional nature of the breaking roller propagation.

## 5.2. Bore front celerity

The average celerity of the median bore front was calculated over longitudinal sections of the channel as  $U_m = \Delta X/\Delta t$ , where  $\Delta X = 0.02$  m was chosen to provide sufficient details of the evolution of the front celerity with time. Results are presented in normalised form in Fig. 15, where the grey areas indicate the intervals during which the roller toe perimeter data set was incomplete within the measurement window. One can notice a constant behaviour associated with smaller Froude numbers, whereas for higher values, a more intense fluctuating behaviour becomes predominant. This is somehow in contrast with the findings of Yeh and Mok [42], who showed lesser fluctuations for increasing Froude numbers in dam break waves propagating over an initial still water layer.

The large amount of details derived from the high-speed videos allowed for a detailed investigation of the instantaneous bore front celerity. These instantaneous values were computed at every location using the displacement of the roller toe between two consecutive frames

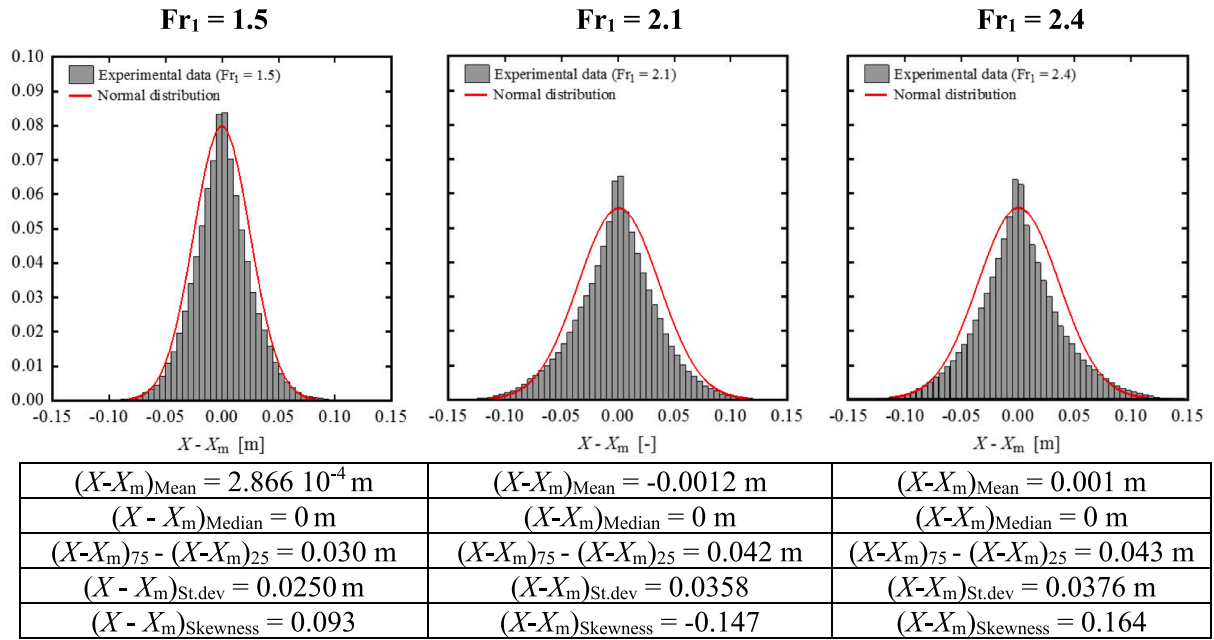


Fig. 12. Probability Distribution Functions of the fluctuations of the roller toe from its median value.

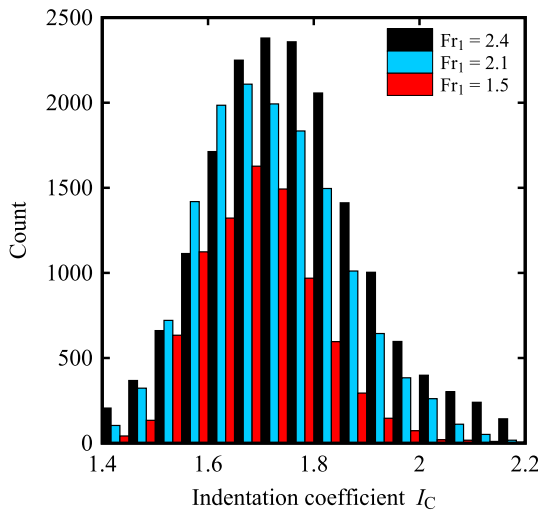


Fig. 13. Statistical distribution of the Indentation coefficient  $I_C$  for different Froude numbers.

( $U = \Delta X/\Delta T$ , where  $\Delta T = 1/1000$  fps). The precision of these data was linked to the pixel size, leading to a mean standard error of  $\pm 0.13$  m/s. All data was filtered of its extreme values and summarized in the PDFs presented in Fig. 16. All configurations revealed a statistical distribution characterised by mean celerity values comparable to the ADM data, showing once again a good agreement between both approaches. In addition, results showed a wide range of instantaneous celerities with a difference in third and first quartile  $U_{75-25}$  between 1.082 m/s for  $Fr_1 = 1.5$  and 1.236 m/s for  $Fr_1 = 2.4$ . The increasing range of celerities is once again a confirmation of the stronger turbulent behaviour associated with higher Froude numbers. All flow conditions showed a negative skewness, implying a longer tail in the negative direction. These negative instantaneous celerities are considered to be responsible for the local backshifts of the roller toe previously discussed. In line with Fig. 12, the PDFs of the instantaneous celerities are compared with a normal distributions with identical mean values and standard deviations. Results showed a substantial deviation from the Gaussian bell-shape for all Froude numbers, thus indicating a non-linear behaviour of

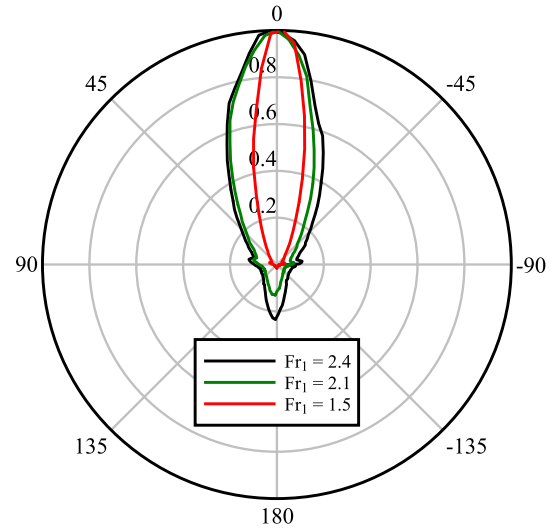


Fig. 14. Local and instantaneous direction of the bore front, where  $\theta = 0^\circ$  represents the upstream direction.

the process. Similarly to the fluctuations of the toe perimeter, the repartition of the instantaneous celerity in 7 transversal section of the channel is detailed in Figure I.3 of the Supplementary Material presented in Appendix B. The results showed no difference in the transversal direction, implying a quasi-uniformity of the bore.

## 6. Discussion

The breaking roller of surges and bores is a complex phenomenon associated with rapid changes, strong turbulence and an oscillatory behaviour. Leng and Chanson [20] observed a characteristic transverse wave length of the roller toe perimeter of about 1.2 times the initial flow depth  $d_1$ . Although this result is consistent with present visual observations, a spectral analysis of the roller toe profiles did not reveal any dominant frequency in the present data. Yet the roller toe perimeter data visually showed a pseudo-cyclic behaviour, which was difficult to quantify due to the turbulent nature of the process. Some specific in-depth analysis of the present data was performed to identify any

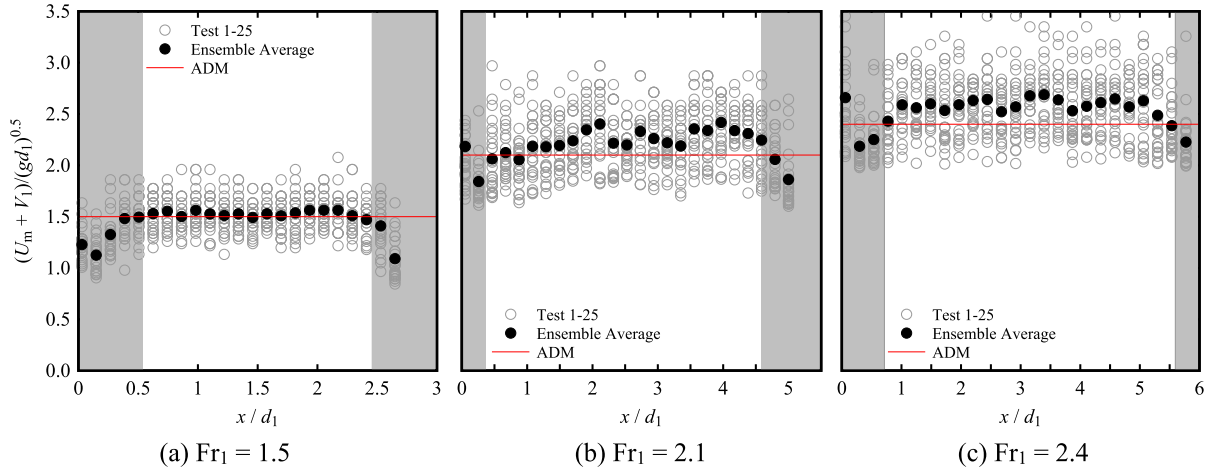


Fig. 15. Normalised celerity values of the median bore front, computed over sections of 0.02 m. Grey areas represent intervals during which the roller toe perimeter was incomplete within the measurement window.

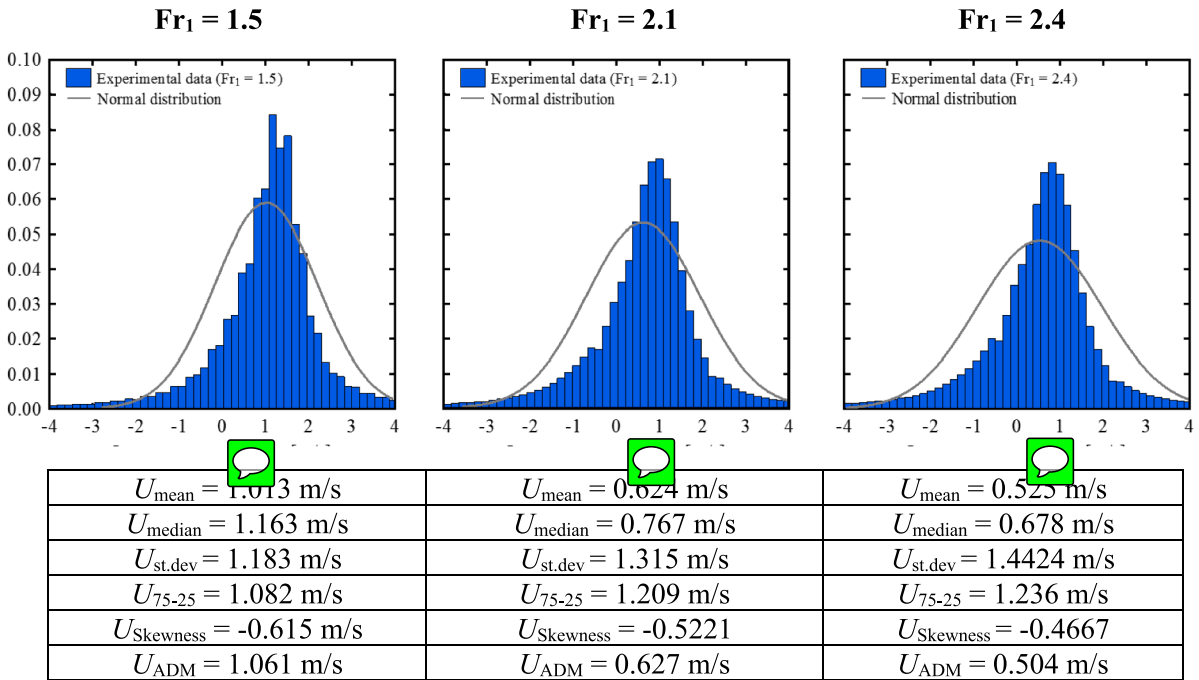


Fig. 16. Statistical distribution of the instantaneous bore front celerity (25 repetitions) and comparison with the normal Gaussian distribution.

periodicity associated with the streamwise motion of the roller toe. A cross correlation between one reference profile  $X(\tau)$  and all subsequent ones  $X(\tau + \Delta\tau)$  was computed as:

$$R_{xy} = \frac{\sum X(\tau) \cdot X(t + \tau)}{\sqrt{\sum X^2(\tau) \cdot X^2(t + \tau)}} \quad (7)$$

The choice of the reference profile  $X(\tau)$  was of critical importance for such an analysis, leading to very heterogeneous results. The process is influenced by a certain degree of randomness, although some of the repetitions showed some periodicity, as shown in Fig. 17. The ensemble-average of all tests with a cyclic behaviour showed a repeating pattern with some dimensionless periods of  $t(g/d_1)^{0.5} = 1.52, 2.92$  and  $4.32$  for  $Fr_1 = 1.5, 2.1$  and  $2.4$ , respectively. This corresponded to durations of about 0.2 s, 0.3 s and 0.4 s in dimensional form. Despite these results, the cyclic behaviour of breaking bores remains hard to assess and a longer signal would be beneficial for a more detailed

analysis. However, the unsteadiness of the process and the translating nature of the bore make such long-duration data very-difficult to acquire.

## 7. Conclusion

Breaking surges and bores are the result of a sudden increase in water depth, generating a complex and highly turbulent front in the form of an aerated and recirculating roller. The present experimental study employed high speed image processing techniques to fully characterize the spatial and temporal dynamics of the bore roller as well as their air-entrainment mechanisms. The experimental investigation of the bore roller with high speed videos from both side and top views allowed for a comprehensive and 3-dimensional characterisation of the bore's front properties, based on a large number of repetitions and ensemble average analysis.

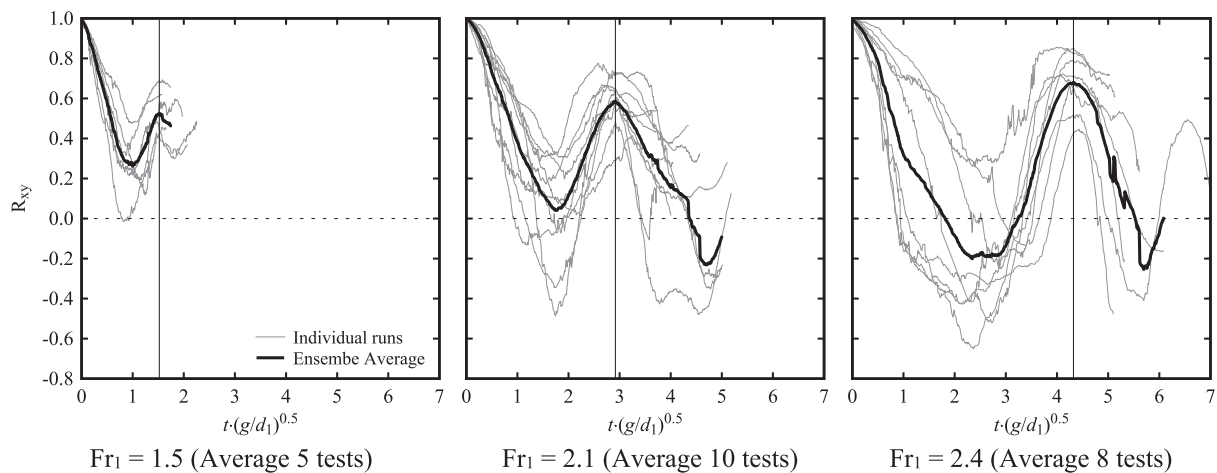


Fig. 17. Cross correlation signal for the profiles of the roller toe. Thin lines represent individual tests, the thick line represents the Ensemble Averaged value of all tests.

Visual observations pointed out different air-entrainment mechanisms for increasing Froude numbers. Weaker bores ( $Fr_1 \sim 1.5$ ) had a shear layer located above the initial free-surface with air-entrainment localised at the roller toe, with entrapment of air pockets subsequently advected downstream. For stronger bores ( $Fr_1 > 2$ ) the shear layer extended below the initial water level, with air-entrainment observed throughout the roller, associated with large-scale turbulent structures leading to intense free-surface fluctuations and ejections. A detailed characterisation of the roller's upper and lower boundaries, showed good agreement between the image processing technique, ADM measurements and previous studies, providing new adapted formulae to estimate the air-water boundary and the extension of the shear layer.

Image processing of the top view video analysis allowed for a detailed recognition of the bore roller toe, analysing its main characteristics in both space and time. Ensemble averaged values of the celerity of the median front was well in agreement with the ADM and side-view measurements. The roller toe presented an indented profile, with an instantaneous perimeter length around 1.7 times the channel width with a quasi-two-dimensional evolution and no significant sidewall effect. Higher Froude numbers were associated with longer turbulent scales and a more intense bi-dimensional behaviour with in-plane movements of the roller toe, deviating from the longitudinal trajectory. In addition, local backshifts of the front were observed as a result of the cyclic, recirculating motion. The high acquisition frequency allowed for a detailed characterisation of the fluctuations of the roller toe and instantaneous wave front celerities, showing some typical statistical distributions with a uniform repartition across the channel width. Preliminary analysis in terms of periodicity associated with the

streamwise motion of the roller toe showed some cyclic behaviour. However, this remains hard to assess, stressing the need for further long-duration and high-quality experimental data for a better understanding of the overall process.

Although limited to one discharge, it is believed that the current analysis provides a insight of the turbulent behaviour and three-dimensional properties of breaking bore roller. While these results will need further developments, experimental studies should be undertaken to characterise the two-phase flow properties and air-water flow features of the propagating roller. Detailed CFD modelling would further be another research focus for which the present data set may provide a validation database.

#### Declaration of Competing Interest

The authors declare that they have no known competing financial interests or personal relationships that could have appeared to influence the work reported in this paper.

#### Acknowledgements

The authors acknowledge helpful discussions with Dr Xinqian (Sophia) Leng as well as the technical assistance of Jason Van Der Gevel and Stewart Matthews (The University of Queensland). The financial support of the Swiss National Science Foundation (grant P2ELP2\_181794) and of the University of Queensland, School of Civil Engineering is acknowledged.

#### Appendix A. Roller characteristics in the transversal direction

This Appendix focuses on the behaviour of the main characteristics of the breaking roller in the transversal direction, i.e. perpendicularly to the flow direction. For this, the channel width (0.7 m) was subdivided in 7 sections with an individual width of  $\Delta y = 0.1$  m (Figure 2a, right). The positions of the median bore front, the roller toe fluctuations and the instantaneous wave front celerities were analysed for each sections, providing a more detailed characterization of the roller properties in the spatial domain. This additional analysis proved that the bores had a uniform behaviour across the channel width. Due to the large amount of data, the results are presented in the Supplementary Material I attached to the main article. It is believed that this specific analysis provides a more comprehensive insight of the turbulent behaviour of breaking bores. This database of experimental data will be useful to numerical modelling in terms of the validations and/or calibrations of numerical models.

#### Appendix B. Movies of breaking bores (digital appendix)

This appendix presents the details of 6 videos of breaking bores, provided as visual support in the understanding of the turbulent processes discussed in the manuscript. All videos were recorded using a Phantom high-speed digital camera (v2011) with a resolution of  $1280 \times 800$ .

**Table B.1**

Details on the videos provide as supplementary material.

Video name	Description	Flow conditions	Native movie format	Video movie format
Bore_Side_1	Side view	Fr = 1.5 $Q = 0.1 \text{ m}^3/\text{s}$ , $h_1 = 0.168 \text{ m}$ $S_0 = 0.00 \%$ , $U = 1.06 \text{ m/s}$	22,000 fps Full HD (1280 × 800)	Frame rate: 100 fps Replayed at 5 fps Full HD (1280 × 800) Duration: 16 s
Bore_Side_2	Side view	Fr = 2.1 $Q = 0.1 \text{ m}^3/\text{s}$ , $h_1 = 0.097 \text{ m}$ $S_0 = 0.75 \%$ , $U = 0.63 \text{ m/s}$	22,000 fps Full HD (1280 × 800)	Frame rate: 100 fps Replayed at 5 fps Full HD (1280 × 800) Duration: 21 s
Bore_Side_3	Side view	Fr = 2.4 $Q = 0.1 \text{ m}^3/\text{s}$ , $h_1 = 0.084 \text{ m}$ $S_0 = 1.25 \%$ , $U = 0.50 \text{ m/s}$	22,000 fps Full HD (1280 × 800)	Frame rate: 100 fps Replayed at 5 fps Full HD (1280 × 800) Duration: 21 s
Bore_Top_1	Top view	Fr = 1.5 $Q = 0.1 \text{ m}^3/\text{s}$ , $h_1 = 0.168 \text{ m}$ $S_0 = 0.00 \%$ , $U = 1.06 \text{ m/s}$	22,000 fps Full HD (1280 × 800)	Frame rate: 100 fps Replayed at 5 fps Full HD (1280 × 800) Duration: 17 s
Bore_Top_2	Top view	Fr = 2.1 $Q = 0.1 \text{ m}^3/\text{s}$ , $h_1 = 0.097 \text{ m}$ $S_0 = 0.75 \%$ , $U = 0.63 \text{ m/s}$	22,000 fps Full HD (1280 × 800)	Frame rate: 100 fps Replayed at 5 fps Full HD (1280 × 800) Duration: 25 s
Bore_Top_3	Top view	Fr = 2.4 $Q = 0.1 \text{ m}^3/\text{s}$ , $h_1 = 0.084 \text{ m}$ $S_0 = 1.25 \%$ , $U = 0.50 \text{ m/s}$	22,000 fps Full HD (1280 × 800)	Frame rate: 100 fps Replayed at 5 fps Full HD (1280 × 800) Duration: 26 s

Note:  $Q$  = discharge,  $h_1$  = upstream water depth,  $S_0$  = channel slope,  $U$  = bore front celerity.

## Appendix C

Supplementary data to this article can be found online at <https://doi.org/10.1016/j.expthermflusci.2019.109980>.

## References

- [1] F. Benet, J.A. Cunge, Analysis of experiments on secondary undulations caused by surge waves in trapezoidal channels, *J. Hydraul. Res.* 9 (1) (1971) 11–33, <https://doi.org/10.1080/00221687109500335>.
- [2] T.B. Benjamin, M.J. Lighthill, On cnoidal waves and bores, *Proc. Royal Soc. A: Mathem., Phys. Eng. Sci.* 224 (1159) (1954) 448–460.
- [3] C.E. Blenkinsopp, J.R. Chaplin, Void fraction measurements in breaking waves, *Proc. Royal Soc. A: Mathem., Phys. Eng. Sci.* 463 (2088) (2007) 3151–3170, <https://doi.org/10.1098/rspa.2007.1901>.
- [4] M. Brocchini, D.H. Peregrine, The dynamics of strong turbulence at free surfaces. Part 2. Free-surface boundary conditions, *J. Fluid Mech.* 449 (2001) 255–290, <https://doi.org/10.1017/S0022112001006024>.
- [5] M. Brocchini, D.H. Peregrine, The dynamics of strong turbulence at free surfaces. Part 1. Description, *J. Fluid Mech.* 449 (2001) 225–254, <https://doi.org/10.1017/S0022112001006012>.
- [6] Y. Chachereau, H. Chanson, Free-surface fluctuations and turbulence in hydraulic jumps, *Exp. Therm. Fluid Sci.* 35 (6) (2011) 896–909, <https://doi.org/10.1016/j.expthermflusci.2011.01.009>.
- [7] H. Chanson, Hydraulic jumps: turbulence and air bubble entrainment, *La Houille Blanche* 3 (2011) 5–16, <https://doi.org/10.1051/lhb/2011026>.
- [8] H. Chanson, Y.H. Toi, Physical modelling of breaking tidal bores: comparison with prototype data, *J. Hydraul. Res.* 53 (2) (2015) 264–273, <https://doi.org/10.1080/00221686.2014.989458>.
- [9] H. Chanson, D. Reungoat, B. Simon, P. Lubin, High-frequency turbulence and suspended sediment concentration measurements in the Garonne River tidal bore, *Estuar. Coast. Shelf Sci.* 95 (2–3) (2011) 298–306, <https://doi.org/10.1016/j.ecss.2011.09.012>.
- [10] D.Du. Fan, G.F. Cai, S. Shang, Y.J. Wu, Y.W. Zhang, L. Gao, Sedimentation processes and sedimentary characteristics of tidal bores along the north bank of the Qiantang Estuary, *Chin. Sci. Bull.* 57 (13) (2012) 1578–1589, <https://doi.org/10.1007/s11434-012-4993-6>.
- [11] H. Favre, *Etude Théorique et Expérimentale des Ondes de Translation dans les Canaux Découverts*. (Theoretical and Experimental Study of Travelling Surges in Open Channels.), *Dunod*, Paris (1935) (in French).
- [12] M.M. Gibson, W. Rodi, Simulation of free surface effects on turbulence with a Reynolds stress model, *J. Hydraul. Res.* 27 (2) (1989) 233–244, <https://doi.org/10.1080/00221688909499183>.
- [13] W.H. Hager, R. Bremen, N. Kawagoshi, Classical hydraulic jump: length of roller, *J. Hydraul. Res.* 28 (1990) 591–608, <https://doi.org/10.1080/00221689009499048>.
- [14] R.A. Handler, T.F. Swean, R.I. Leighton, J.D. Swearingen, Length scales and the energy balance for turbulence near a free surface, *AIAA J.* 31 (11) (1993) 1998–2007.
- [15] F.M. Henderson, *Open Channel Flow, Second Edition, Handbook of Fluid Dynamics*, 1966.
- [16] H.G. Hornung, C. Willert, S. Turner, The flow field downstream of a hydraulic jump, *J. Fluid Mech.* 287 (1995) 299–316, <https://doi.org/10.1017/S0022112095000966>.
- [17] J.W. Hoyt, R.H.J. Sellin, Hydraulic Jump as “mixing layer”, *J. Hydraul. Eng.* 115 (1989) 1607–1614, [https://doi.org/10.1061/\(asce\)0733-9429\(1989\)115:12\(1607\)](https://doi.org/10.1061/(asce)0733-9429(1989)115:12(1607)).
- [18] N. Khezri, H. Chanson, Sediment inception under breaking tidal bores, *Mech. Res. Commun.* 41 (2012) 49–53, <https://doi.org/10.1016/j.mechrescom.2012.02.010>.
- [19] Leng, X., (2018). A Study of Turbulence: the Unsteady Propagation of Bores and Surges. PhD Thesis, The University of Queensland, 364 pages. (DOI: 10.14264/uql.2018.501).
- [20] X. Leng, H. Chanson, Breaking bore: physical observations of roller characteristics, *Mech. Res. Commun.* 65 (2015) 24–29, <https://doi.org/10.1016/j.mechrescom.2015.02.008>.
- [21] X. Leng, H. Chanson, Turbulent advances of a breaking bore: preliminary physical experiments, *Exp. Therm. Fluid Sci.* 62 (2015) 70–77, <https://doi.org/10.1016/j.expthermflusci.2014.12.002>.
- [22] X. Leng, H. Chanson, Unsteady turbulence, dynamic similarity and scale effects in bores and positive surges, *Europ. J. Mech., B/Fluids* 61 (2017) 125–134, <https://doi.org/10.1016/j.euromechflu.2016.09.017>.
- [23] X. Leng, H. Chanson, Two-dimensional integral turbulent scales in compression wave in a canal, *Exp. Therm. Fluid Sci.* 102 (2019) 163–180, <https://doi.org/10.1016/j.expthermflusci.2018.09.014>.
- [24] X. Leng, B. Simon, N. Khezri, P. Lubin, H. Chanson, CFD modeling of tidal bores: development and validation challenges, *Coastal Eng. J.* 60 (4) (2018) 423–436, <https://doi.org/10.1080/21664250.2018.1498211>.
- [25] P. Lubin, S. Glockner, Numerical simulations of three-dimensional plunging breaking waves: generation and evolution of aerated vortex filaments, *J. Fluid Mech.* 767 (2015) 364–393, <https://doi.org/10.1017/jfm.2015.62>.
- [26] P. Lubin, H. Chanson, S. Glockner, Large Eddy Simulation of turbulence generated by a weak breaking tidal bore, *Environ. Fluid Mech.* 10 (5) (2010) 587–602, <https://doi.org/10.1007/s10652-009-9165-0>.
- [27] P.A. Madsen, H.J. Simonsen, C.H. Pan, Numerical simulation of tidal bores and hydraulic jumps, *Coast. Eng.* 52 (5) (2005) 409–433, <https://doi.org/10.1016/j.coastaleng.2004.12.007>.
- [28] D. Mouaze, F. Murzyn, J.R. Chaplin, Free surface length scale estimation in hydraulic jumps, *J. Fluids Eng.* 127 (6) (2005) 1191, <https://doi.org/10.1115/1.2060736>.
- [29] F. Murzyn, H. Chanson, Two-phase gas-liquid flow properties in the hydraulic jump: review and perspectives, *Multiphase Flow Res.* (2009) 497–542.
- [30] B. Na, K.-A. Chang, Z.C. Huang, H.J. Lim, Turbulent flow field and air entrainment in laboratory plunging breaking waves, *J. Geophys. Res. Oceans* 121 (2016) 2980–3009, <https://doi.org/10.1002/2015JC011377>.
- [31] C.-H. Pan, B.-Y. Lin, X.-Z. Mao, Case study: numerical modeling of the tidal bore on

- the Qiantang river, China, *J. Hydraulic Eng.* 133 (2) (2007) 130–138, [https://doi.org/10.1061/\(ASCE\)0733-9429\(2007\)133:2\(130\)](https://doi.org/10.1061/(ASCE)0733-9429(2007)133:2(130)).
- [32] D.H. Peregrine, Calculations of development of an undular bore, *J. Fluid Mech.* 25 (2) (1966) 321–330, <https://doi.org/10.1017/S0022112066001678>.
- [33] D. Reungoat, H. Chanson, C.E. Keevil, Field measurements of unsteady turbulence in a tidal bore: the Garonne river in October 2013, *J. Hydraul. Res.* 53 (3) (2015) 291–301, <https://doi.org/10.1080/00221686.2015.1021717>.
- [34] D. Reungoat, P. Lubin, X. Leng, H. Chanson, Tidal bore hydrodynamics and sediment processes: 2010–2016 field observations in France, *Coastal Eng. J.* 60 (4) (2018) 484–498, <https://doi.org/10.1080/21664250.2018.1529265>.
- [35] M.A.C. Teixeira, S.E. Belcher, On the distortion of turbulence by a progressive surface wave, *J. Fluid Mech.* 458 (2002) 229–267, <https://doi.org/10.1017/S0022112002007838>.
- [36] Wang, H., (2014). Turbulence air entrainment in Hydraulic Jumps. PhD Thesis, The University of Queensland, 341 pages. (DOI: 10.14264/uq.2014.542).
- [37] H. Wang, H. Chanson, Air entrainment and turbulent fluctuations in hydraulic jumps, *Urban Water J.* 12 (6) (2015) 502–518, <https://doi.org/10.1080/1573062X.2013.847464>.
- [38] H. Wang, F. Murzyn, H. Chanson, Interaction between free-surface, two-phase flow and total pressure in hydraulic jump, *Exp. Therm. Fluid Sci.* 64 (2015) 30–41, <https://doi.org/10.1016/j.expthermflusci.2015.02.003>.
- [39] D. Wilkinson, M. Banner, Undular bores, *Austral. Fluid Mech. Conf.* (1977) 369–373.
- [40] D. Wüthrich, M. Pfister, I. Nistor, A.J. Schleiss, Experimental study of tsunami-like waves generated with a vertical release technique on dry and wet beds, *J. Waterw. Port Coastal Ocean Eng.* 144 (4) (2018) 04018006, [https://doi.org/10.1061/\(ASCE\)WW.1943-5460.0000447](https://doi.org/10.1061/(ASCE)WW.1943-5460.0000447).
- [41] H. Yasuda, One-Dimensional study on propagation of tsunami wave in river channels, *J. Hydraul. Eng.* 136 (2) (2010) 93–105, [https://doi.org/10.1061/\(ASCE\)HY.1943-7900.0000150](https://doi.org/10.1061/(ASCE)HY.1943-7900.0000150).
- [42] H.H. Yeh, K.M. Mok, On turbulence in bores, *Phys. Fluids A* 2 (5) (1990) 821–828, <https://doi.org/10.1063/1.857630>.
- [43] G. Zhang, H. Wang, H. Chanson, Turbulence and aeration in hydraulic jumps: free-surface fluctuation and integral turbulent scale measurements, *Environ. Fluid Mech.* 13 (2) (2013) 189–204, <https://doi.org/10.1007/s10652-012-9254-3>.
- [44] F. Zonta, A. Soldati, M. Onorato, Growth and spectra of gravity-capillary waves in counter current air/water turbulent flow, *J. Fluid Mech.* 777 (2015) 245–259, <https://doi.org/10.1017/jfm.2015.356>.

WÜTHRICH, D., SHI, R., and CHANSON, H. (2020). "Physical Study of the 3-dimensional Characteristics and Free-surface Properties of a Breaking Roller in Bores and Surges." *Experimental Thermal and Fluid Science*, Vol. 112, Paper 109980, 13 pages, Supplementary material (4 pages) & 6 video movies (DOI: 10.1016/j.expthermflusci.2019.109980) (ISSN 0894-1777).

## PHYSICAL STUDY OF THE 3-DIMENSIONAL CHARACTERISTICS AND FREE-SURFACE PROPERTIES OF A BREAKING ROLLER IN BORES AND SURGES

Davide WÜTHRICH, corresponding author.

Post-Doctoral researcher, The University of Queensland, School of Civil Engineering, Brisbane QLD 4072, Australia. Email: [d.wuthrich@uq.edu.au](mailto:d.wuthrich@uq.edu.au)

Rui SHI

Doctoral student, The University of Queensland, School of Civil Engineering, Brisbane, QLD 4072, Australia. Email: [rui.shi@uq.net.au](mailto:rui.shi@uq.net.au)

Hubert CHANSON

Professor, The University of Queensland, School of Civil Engineering, Brisbane, QLD 4072, Australia. Email: [h.chanson@uq.edu.au](mailto:h.chanson@uq.edu.au)

### ORCID Numbers

D. WÜTHRICH:	0000-0003-1974-3560
R. SHI:	0000-0001-9387-9496
H. CHANSON:	0000-0002-2016-9650

## Appendix A - Roller characteristics in the transversal direction

This supplementary material provides additional information on the behaviour of the bore roller in the transversal direction, *i.e.* perpendicular to the flow. This is a relevant issue in physical modelling as well as in practical applications. As shown in Figure 2a (right) of the manuscript, the channel width (0.7 m) was subdivided in 7 sections with an individual width of  $\Delta y = 0.1$  m. All results for all Froude numbers are ensemble averaged over a number of 25 repetitions. The main properties of the bore's roller analysed in Section 5 are herein detailed for each section, providing a more detailed characterization of the roller properties in the spatial domain.

The position of the roller toe for all sections is presented in Figure I.1 along with the median values computed over the whole width. Note that the grey areas indicate the intervals during which the roller toe perimeter is incomplete within the measurement window. Results showed minor differences between all sections, thus highlighting a uniform behaviour of the roller toe throughout the channel width.

WÜTHRICH, D., SHI, R., and CHANSON, H. (2020). "Physical Study of the 3-dimensional Characteristics and Free-surface Properties of a Breaking Roller in Bores and Surges." *Experimental Thermal and Fluid Science*, Vol. 112, Paper 109980, 13 pages, Supplementary material (4 pages) & 6 video movies (DOI: 10.1016/j.expthermflusci.2019.109980) (ISSN 0894-1777).

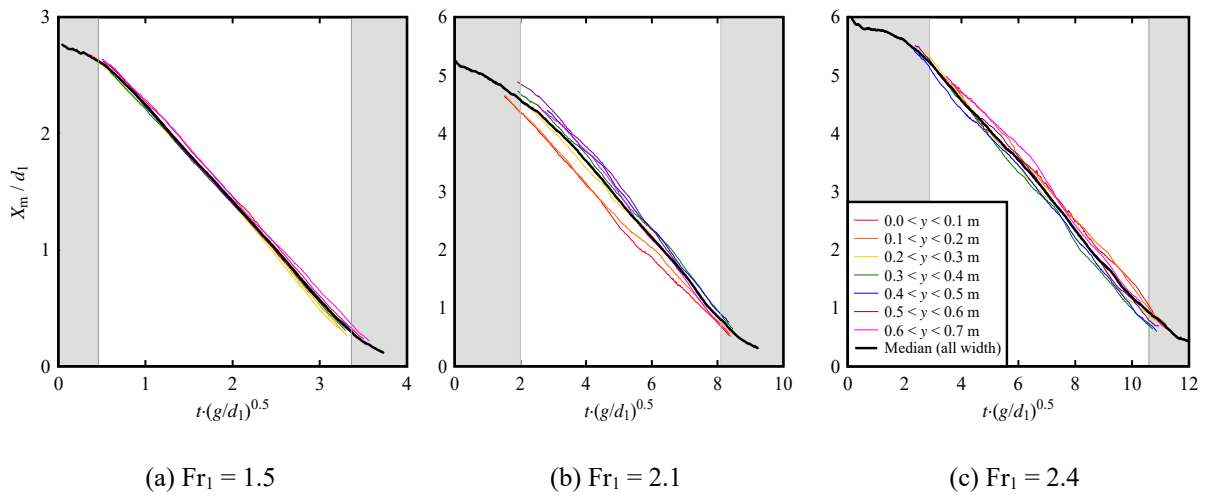


Figure I.1 – Position of roller toes in different sections of the channel for different Froude numbers. (Legend applies to all figures)

The fluctuation of the bore front  $X'$  were computed for each section as  $X' = X - X_m$ , where  $X_m$  is the median value of each section. The main results are presented in the form of statistical distributions in Figure I.2. As compared to the distribution obtained across the whole channel width (Figure 11 of the manuscript), little differences were observed. The instantaneous celerity values were computed for each section of the channel using the displacement of the roller toe between two consecutive frames ( $U = \Delta X / \Delta T$ , where  $\Delta T = 1/1000$  fps), leading to the PDF distributions presented in Figure I.3. Similarly to the fluctuations of the bore front, little differences are observed between the sections, thus confirming the uniform behaviour of the bore characteristics in the transverse direction.

It is believed that this in-depth analysis provides a detailed insight of the turbulent behaviour of breaking bores. This comprehensive experimental data will be useful to numerical modelling in terms of the validations and/or calibrations of numerical models.

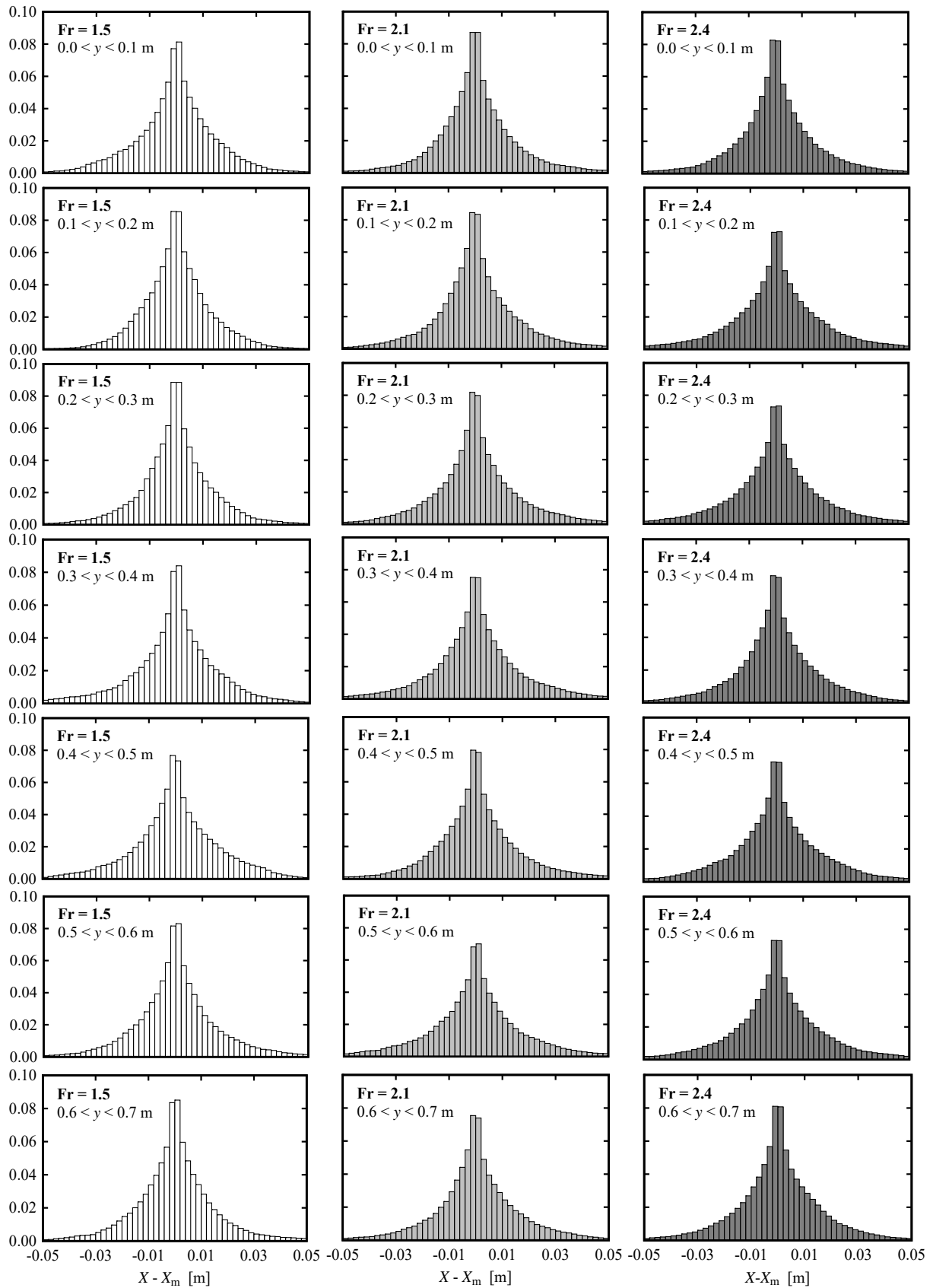


Figure I.2 –Distribution of the fluctuations in the transversal direction (7 sections of 0.1 m, Figure 2a).

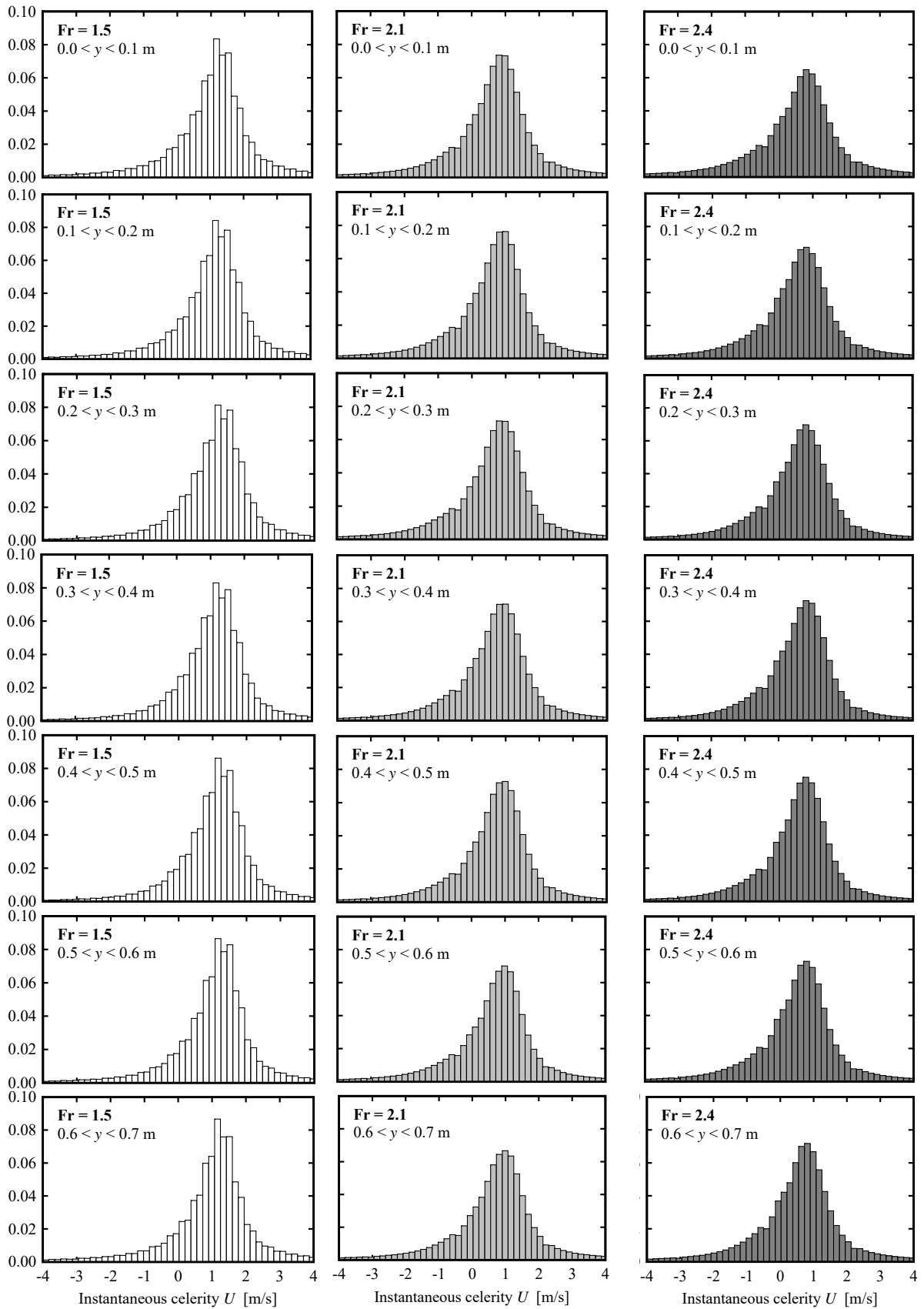


Figure I.3 –Distribution of the instantaneous celerities in the transversal direction (7 sections of 0.1 m, Figure 2a).